Introduction to Stellar Evolution

Erika Bohm-Vitense

University of Washington

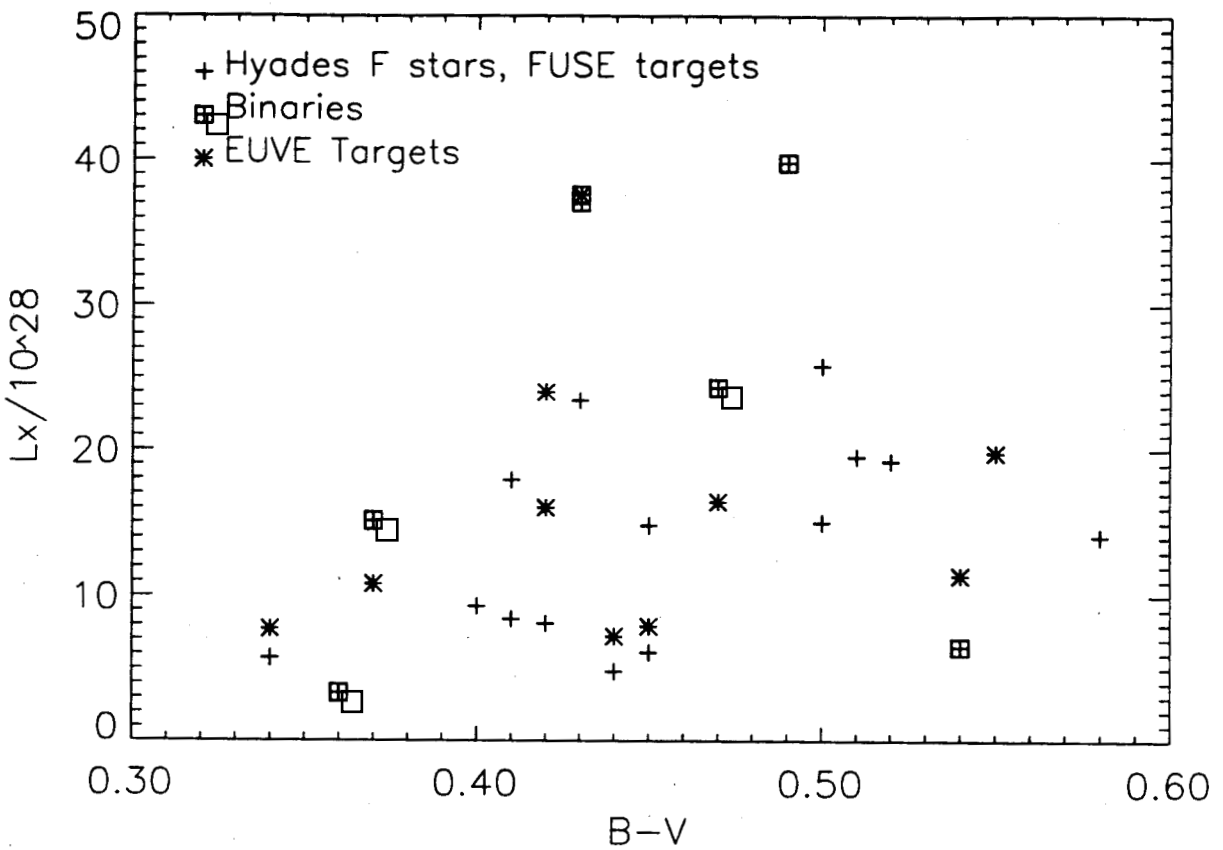
Hyades F stars, FUSE targets
Binaries
EUVE Targets
Lx/10^28
B−V
0
10
20
30
40
50
0.30
0.40
0.50
0.60

Hydrogen Burning

p-p chain

pp I	$H^1 + H^1$	$\rightarrow$	$D^2 + e^+ + \nu$	1.4×10^{10} years	in solar interior
	$D^2 + H^1$	$\rightarrow$	$He^3 + \gamma$	6 sec	$T \sim 1.4 \times 10^6$
	$He^3 + He^3$	$\rightarrow$	$He^4 + H^1 + H^1$	10^6 years	$\rho = 100$ g cm^{-3}
pp II	$He^3 + He^4$	$\rightarrow$	$Be^7 + \gamma$		
	$Be^7 + e^-$	$\rightarrow$	$Li^7 + \nu$	make Li^7, transport	out fast
	$Li^7 + H^1$	$\rightarrow$	$He^4 + He^4$		
pp III	$Be^7 + H^1$	$\rightarrow$	$B^8 + \gamma$		
	B^8	$\rightarrow$	$Be^8 + e^+ + \nu$		
	Be^8	$\rightarrow$	$2He^4$		

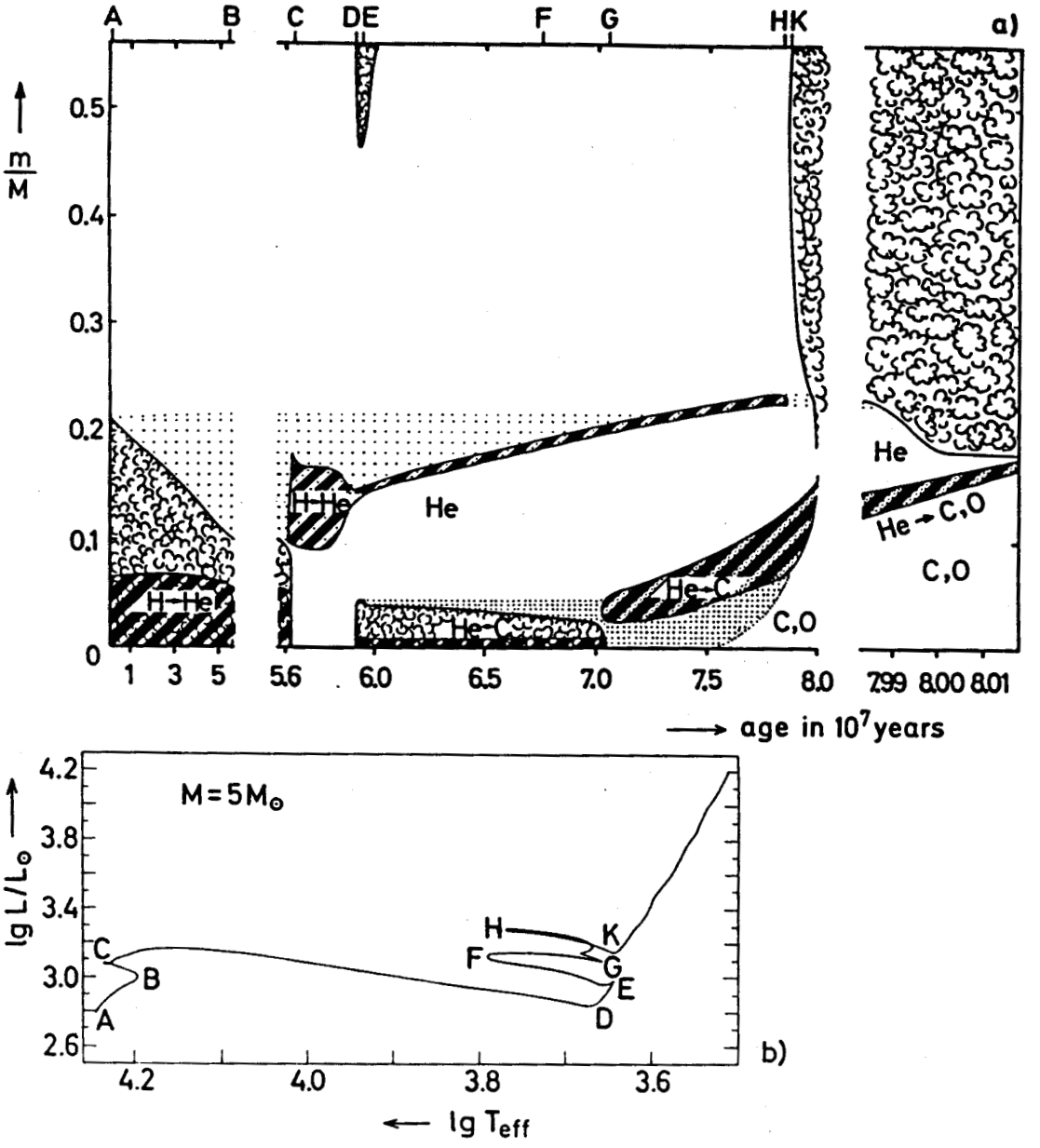

Fig. 31.2. (a) The evolution of the internal structure of a star of $5M_\odot$ of extreme population I. The abscissa gives the age after the ignition of hydrogen in units of 10^7 years; each vertical line corresponds to a model at a given time. The different layers are characterized by their values of m/M. "Cloudy" regions indicate convective areas. Heavily hatched regions indicate where the nuclear energy generation (ε_H or ε_{He}) exceeds 10^3 erg g^{-1} s^{-1}. Regions of variable chemical composition are dotted. The letters $A \ldots K$ above the upper abscissa indicate the corresponding points in the evolutionary track, which is plotted in Fig. 31.2 (b). (After KIPPENHAHN et al., 1965)

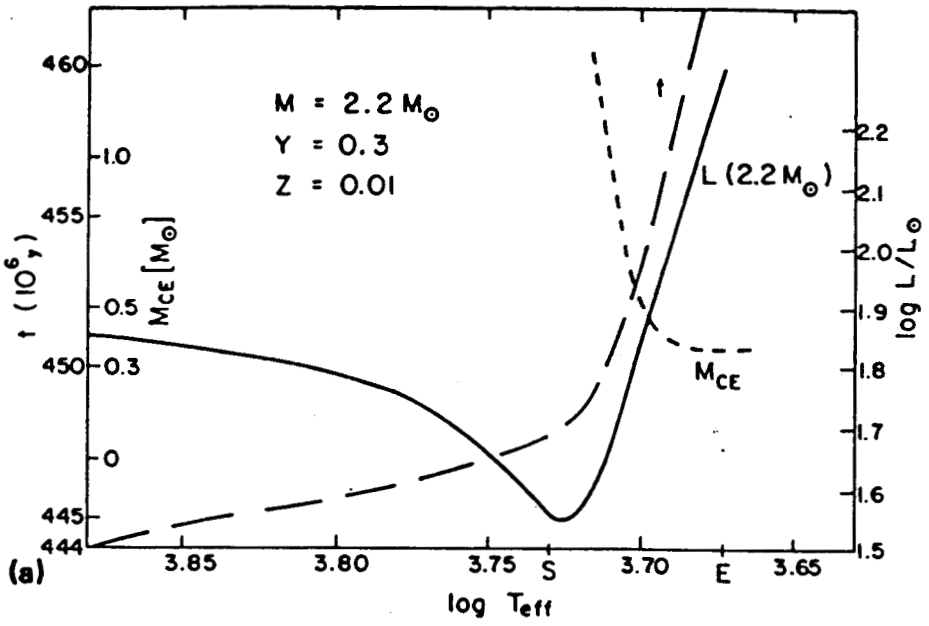
M = 2.2 M⊙
Y = 0.3
Z = 0.01
t
L (2.2 M⊙)
M_CE
t (10^6 y)
M_CE [M⊙]
log L/L⊙
460
455
450
445
444
1.0
0.5
0.3
0
2.2
2.1
2.0
1.9
1.8
1.7
1.6
1.5
3.85
3.80
3.75
S
3.70
E
3.65
log T_eff
(a)

Giants

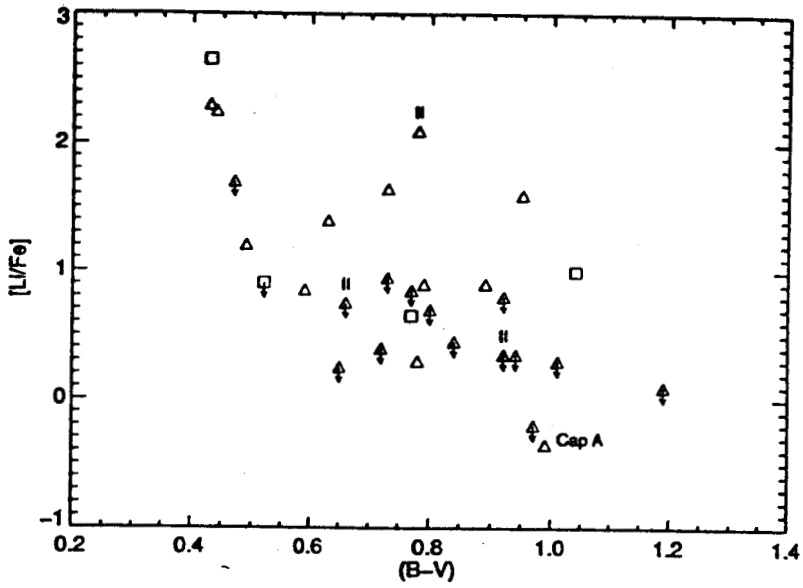

Fig 17

FIG. 6. The logarithmic ratio of [Li/Fe] is plotted against $B-V$ for stars with $v \sin i < 50$ km s^{-1}. The squares indicate likely subgiants. Luminosity class II stars are also indicated. Capella A is noted.

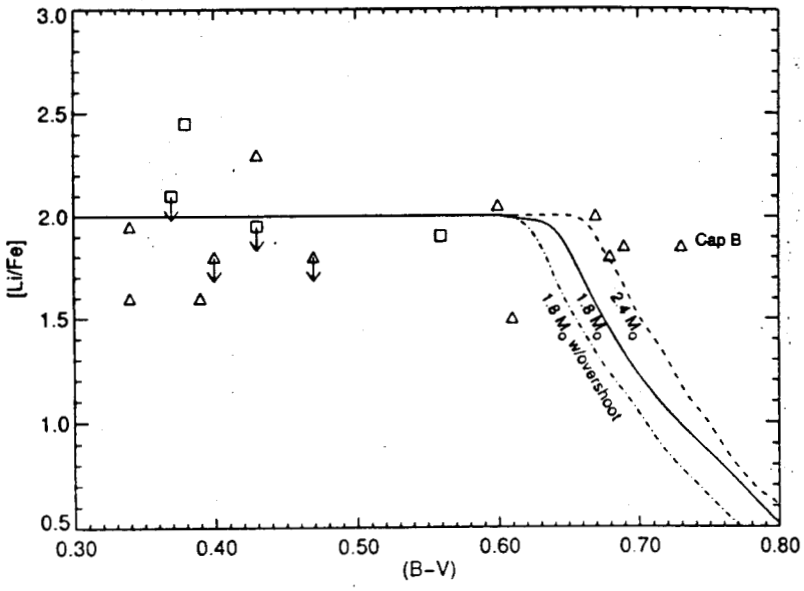

FIG. 4. The logarithmic ratio of [Li/Fe] plotted against $B-V$ for stars wi $v \sin i \geqslant 50$ km s^{-1}. The squares indicate likely subgiants; the triangles a probably giants. The high upper limits due to the difficulty in measuri broad weak lines are to be noticed. Also shown are the theoretical evol tionary curves for the Li abundances for 2.4$\mathscr{M}_\odot$ (dashed curve) and 1.8$\mathscr{M}$ giants without overshoot (solid line) and with one pressure scale hei overshoot (dashed dot line) according to data kindly provided by Swens (1992). The curves were adjusted to match [Li/Fe]=2 for $B-V=0.3$.

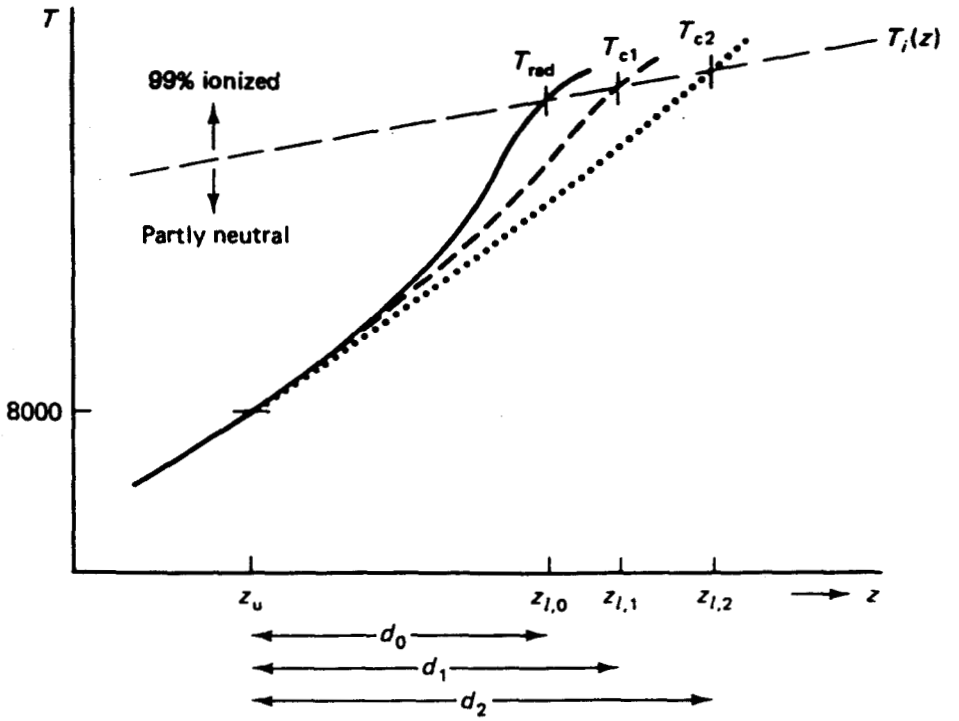

Fig. 7.1. The radiative equilibrium temperature stratification T_{rad} plotted schematically as a function of depth z (solid line). Also shown are qualitatively the temperature stratifications for inefficient convective energy transport, T_{c1} (dashed line), and for efficient convection, T_{c2} (dotted line). Hydrogen and helium are nearly completely ionized for temperatures above a line $T_i(z)$ in the $T(z)$ plane as indicated by the long dashes. (For deeper values with higher P_g, larger T are required according to the Saha equation; see Volume 2.) The intersection of the temperature stratification with this line shows the lower boundary of the hydrogen convection zone. For more efficient convection the boundary occurs at a deeper layer.

Fig 20

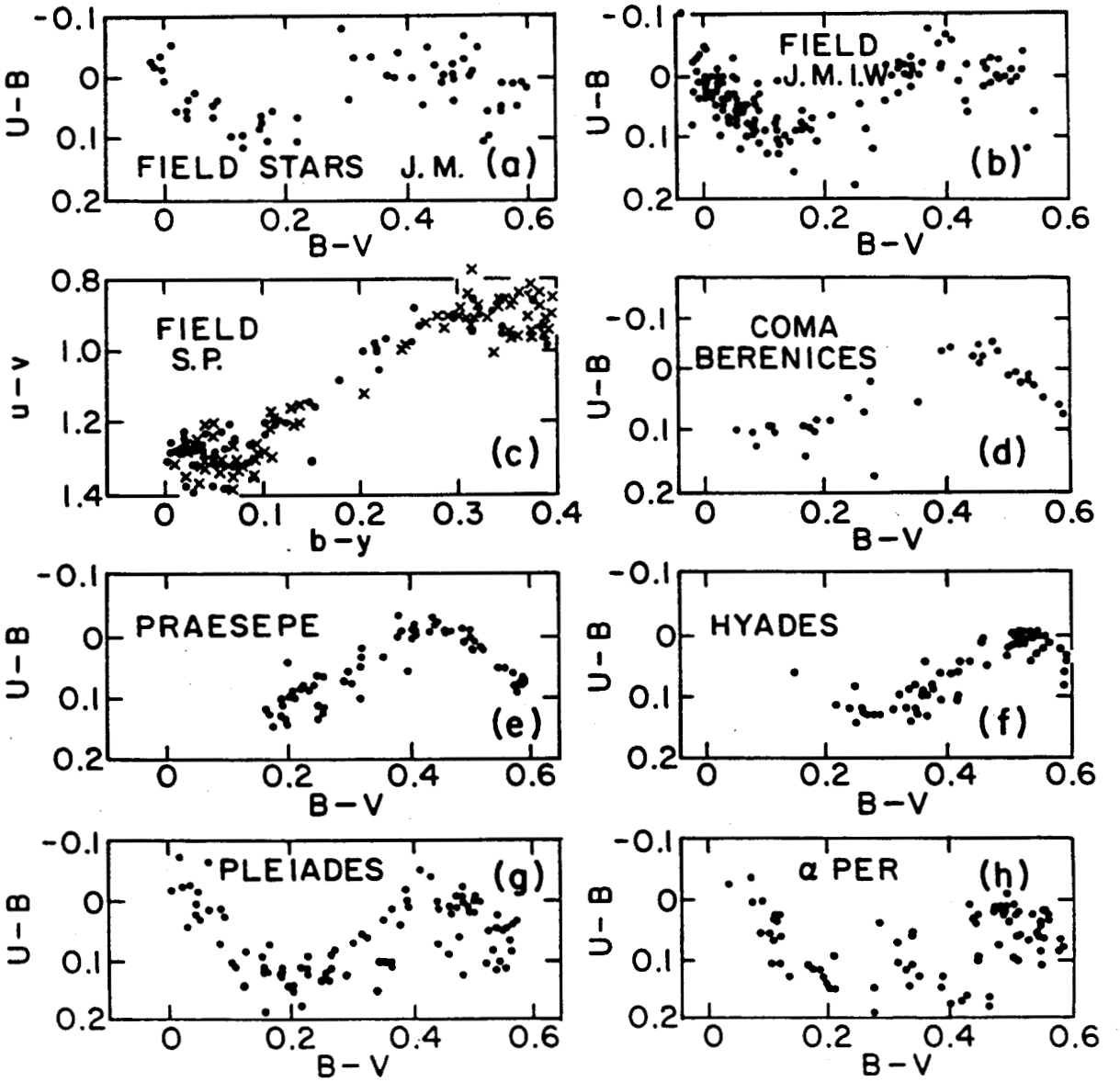

FIG. 1.—Two-color diagrams for the field stars according to Johnson and Morgan (1953). Fig. 1*a*, according to J (1966); fig. 1*b*, according to the Strömgren-Perry catalog (1965); fig. 1*c*, for the Coma Berenices cluster according to Knuckles (1955), for Praesepe according to Johnson (1952), for the Hyades according to Johnson *et al.* (1962), for according to Johnson and Mitchell (1958), and for α Per according to Mitchell (1960). A gap or at least a reduced st obvious for all star groups except for the Pleiades.

The dots in fig. 1*c* designate those stars which are also contained in fig. 1*a* or 1*b*. The crosses are additional stars.

Fig 21

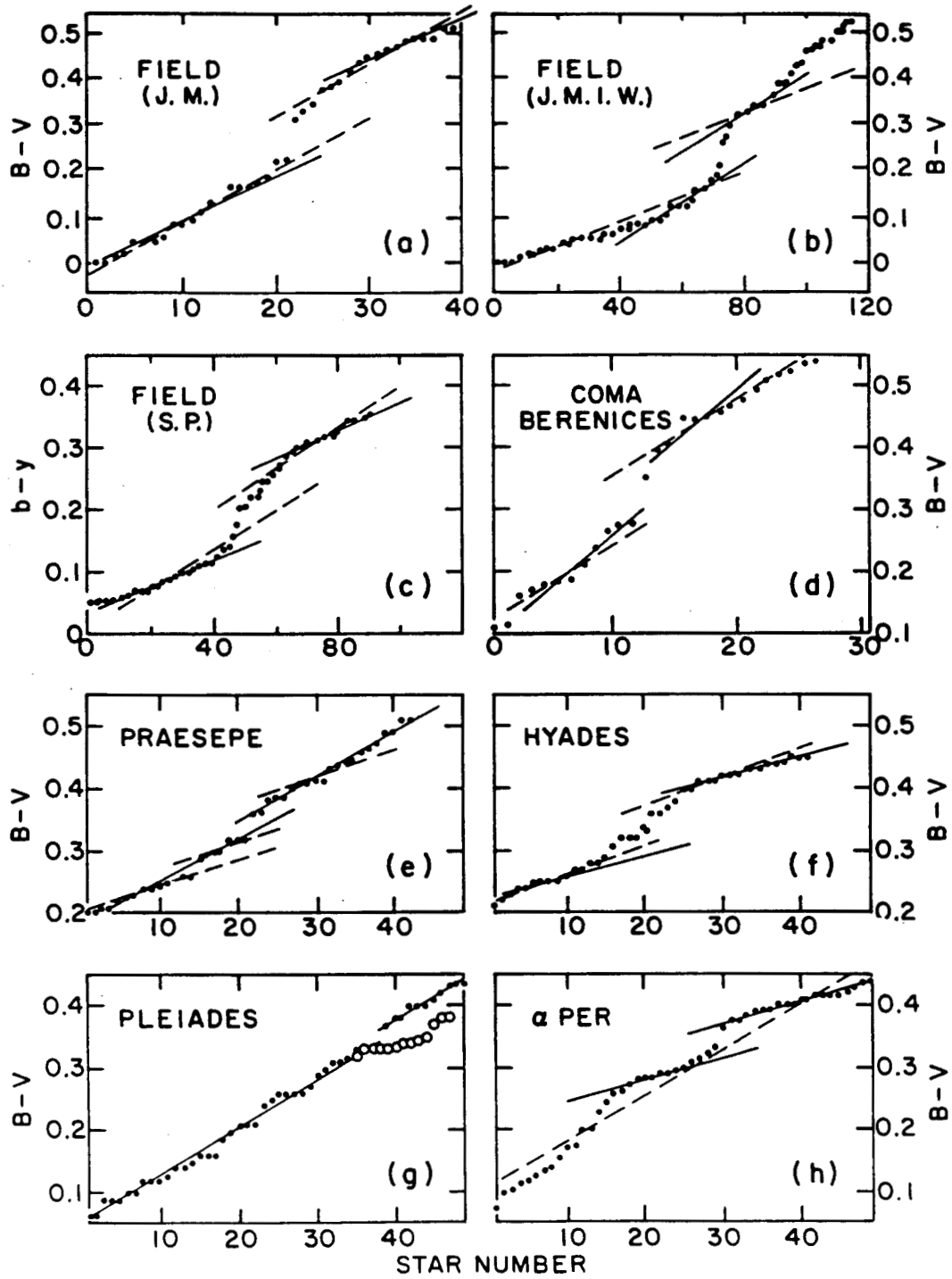

FIG. 2.—Shows the Aizenmann-Demarque-Miller (1969) diagrams for the field stars and the clusters shown in fig. 1. A uniform star distribution over color should result in a straight line. A discontinuous shift in color results in a discontinuous shift of the straight line. These shifts are observed for the field stars, for Coma Bernices, for the Hyades, and possibly for Praesepe. For α Per the situation is unclear; for the Pleiades the shift is not present.

In fig. 1*g*, the dots include stars with $E(B - V) < 0.20$, the circles include stars whose position in the two-color diagrams seems to require $E(B - V) > 0.20$.

Fig 9.1b

References

Books to consult

B\"ohm-Vitense, E. 1992, Introduction to stellar astrophysics, Volume 3, stellar structure and evolution.

Chandrasekhar, S., 1939, An Introduction to the study of stellar structure, University of Chicago Press

Clayton, D.,1983 Principles of stellar evolution and Nucleosynthesis. University of Chicago Press

Cox,J. and Giuli,R., 1968, Stellar structure, vol.1 and vol.2, Gordon and Breach, Bew York

Eddigton,A., 1959, The internal constitution of stars, Dover publ.

Hansen, C.J. and Kawaler, S.D., 1994 , Stellar Interiors, Physical principles, structure, and evolution , Springer Verlag

Kippenhahn, R. and Weigert,A. Stellar structure and evolution, 1990, Springer Verlag

Novotny,E., Introduction to stellar atmospheres and interiors, 1973, Oxford University Press

Schwarzschild, M. Structure and evolution of the stars, 1958, Princeton University Press

Articles and papers

Arp,H.C. 1958, in Handbook of Physics Vol 51, Springer Verlag, p.75

Barnes,G.,Charbonneau,P., and Mc Gregor,K.B. 1999, ApJ 511, 466

Becker, S.A. and Cox,A. 1982, ApJ 260,707

Becker,S.A., Iben,I. and Tuggle,R.S. 1977, ApJ 218,633

Bertelli,G.Bressan,A.G. and Chiosi,C. 1987, A&A 130,279

Boesgaard, A.M. and Trippico,M.J. 1986, ApJ 302, L49

Boesgaard, A.M. and Budge,K. 1988, ApJ 332,410

B\"ohm-Vitense,E. et al., 1998, ApJ 505,903

B\"ohm-Vitense, E. 1995, A&A 297,L25

Burnham,R., 1978,Burnham's Celestial Handbook, Dover Publ. New York, p.1911

Cox,J.P. and Salpeter,E.E. 1964, ApJ 140,485

Gray,D. and Nagar,P. ApJ 298,756,1985

Hayashi,C., 1966 ARAA 4,171

Hesser,J.E. et al. 1987, PASP 99,739

Iben, I.1967, ARAA 5,571

Johnson, H.L. and Morgan, W.W., 1953, ApJ 117, 313

Pinsooneault,M.H. et al. 1999, ApJ 527,180

Popper,D.M. 1980, ARAA 18,115

Roger,F.J. and Iglesias,C.A. ApJS 79,507, 1992

Sandage,A.R. 1986, ARAA 24,450

Simon,N. 1982, ApJ, 260, L87

Stahler, S.W. 1983, ApJ 274,822

Swenson, F. 1992, private communication

Ventura et al. A+A 334,953, 1998

Wallerstein, G. et al. 1994, AJ 107,2211

Hydrogen Burning

p-p chain

pp I	$H^1 + H^1$	$\rightarrow$	$D^2 + e^+ + \nu$	1.4×10^{10} years	in solar interior
	$D^2 + H^1$	$\rightarrow$	$He^3 + \gamma$	6 sec	$T \sim 1.4 \times 10^6$
	$He^3 + He^3$	$\rightarrow$	$He^4 + H^1 + H^1$	10^6 years	$\rho = 100$ g cm^{-3}
pp II	$He^3 + He^4$	$\rightarrow$	$Be^7 + \gamma$		
	$Be^7 + e^-$	$\rightarrow$	$Li^7 + \nu$	make Li^7, transport	out fast
	$Li^7 + H^1$	$\rightarrow$	$He^4 + He^4$		
pp III	$Be^7 + H^1$	$\rightarrow$	$B^8 + \gamma$		
	B^8	$\rightarrow$	$Be^8 + e^+ + \nu$		
	Be^8	$\rightarrow$	$2He^4$		

Hydrogen Burning Cont.

CNO cycle, $\sim 10^7$ K

$C^{12} + H^1$	$\rightarrow$	$N^{13} + \gamma$	10^6 years
N^{13}	$\rightarrow$	$C^{13} + e^+ + \nu$	14 min
$C^{13} + H^1$	$\rightarrow$	$N^{14} + \gamma$	3×10^5 years
$N^{14} + H^1$	$\rightarrow$	$O^{15} + \gamma$	3×10^8 years
O^{15}	$\rightarrow$	$N^{15} + e^+ + \nu$	82 sec
$N^{15} + H^1$	$\rightarrow$	$C^{12} + He^4$	10^4 years

or

$$N^{15} + H^1 \rightarrow O^{16} + \gamma$$

$$O^{16} + H^1 \rightarrow F^{17} + \gamma$$

$$F^{17} \rightarrow O^{17} + e^+ + \nu$$

$$O^{17} + H^1 \rightarrow N^{14} + He^4$$

triple α process = helium burning

$$He^4 + He^4 \leftrightarrow Be^8$$

$$Be^8 + He^4 \rightarrow C^{12} + 2\gamma + 7.6 \text{ MeV} \quad T \sim 10^8 \text{ K}$$

but $He^4 + He^4 \leftrightarrow Be^8 - 95$ keV

Li problem

$$Li^6 + H^1 \rightarrow He^4 + He^3 \quad \text{at } T \sim 2 \times 10^6 \text{ K}$$

$$Li^7 + H^1 \rightarrow 2He^4 \quad \text{at } T \sim 2.4 \times 10^6 \text{ K, i.e., deeper layer}$$

Convective Energy Transport

$$\pi F_c = \rho \overline{v} c_p \Delta T \tag{12}$$

$$\overline{\Delta T} = \left(\overline{\frac{dT}{dz}} - \overline{\frac{dT}{dz_{\mathrm{bu}}}} \right) \frac{l}{2} \qquad l = \text{travel distance} \tag{13}$$

$$v^2(s) = 2g \int_0^s \left[\frac{dT}{dz} - \left(\frac{dT}{dz} \right)_{\mathrm{bu}} \right] \frac{1}{T} s ds = \frac{2g}{T} \left[\frac{dT}{dz} - \left(\frac{dT}{dz} \right)_{\mathrm{bu}} \right] \frac{s^2}{2} \tag{14}$$

$$\text{with} \qquad \overline{s} = \frac{l}{2} \tag{15}$$

$$\pi F_c = \rho c_p T Q \sqrt{g} \frac{\left[\frac{dT}{dz} - \left(\frac{dT}{dz} \right)_{bu} \right]^{3/2}}{T^{3/2}} \left(\frac{l}{2} \right)^2 \tag{16}$$

For efficient convective energy transport

$$\nabla = \nabla_{\mathrm{ad}} \tag{17}$$

Virial Theorem

$$E_{th} = \int_0^R \frac{3}{2} kTn(r) 4\pi r^2 dr = \int_0^R \frac{3}{2} P 4\pi r^2 dr \tag{4}$$

from hydrostatic equilibrium equation

$$-\int_0^R 3P 4\pi r^2 dr = \int_0^R \rho \frac{GM_r}{r} 4\pi r^2 dr \tag{5}$$

$$E_{gr} = -\int_0^R \frac{GM_r}{r} \cdot \rho \cdot 4\pi r^2 dr = -2E_{th} \tag{6}$$

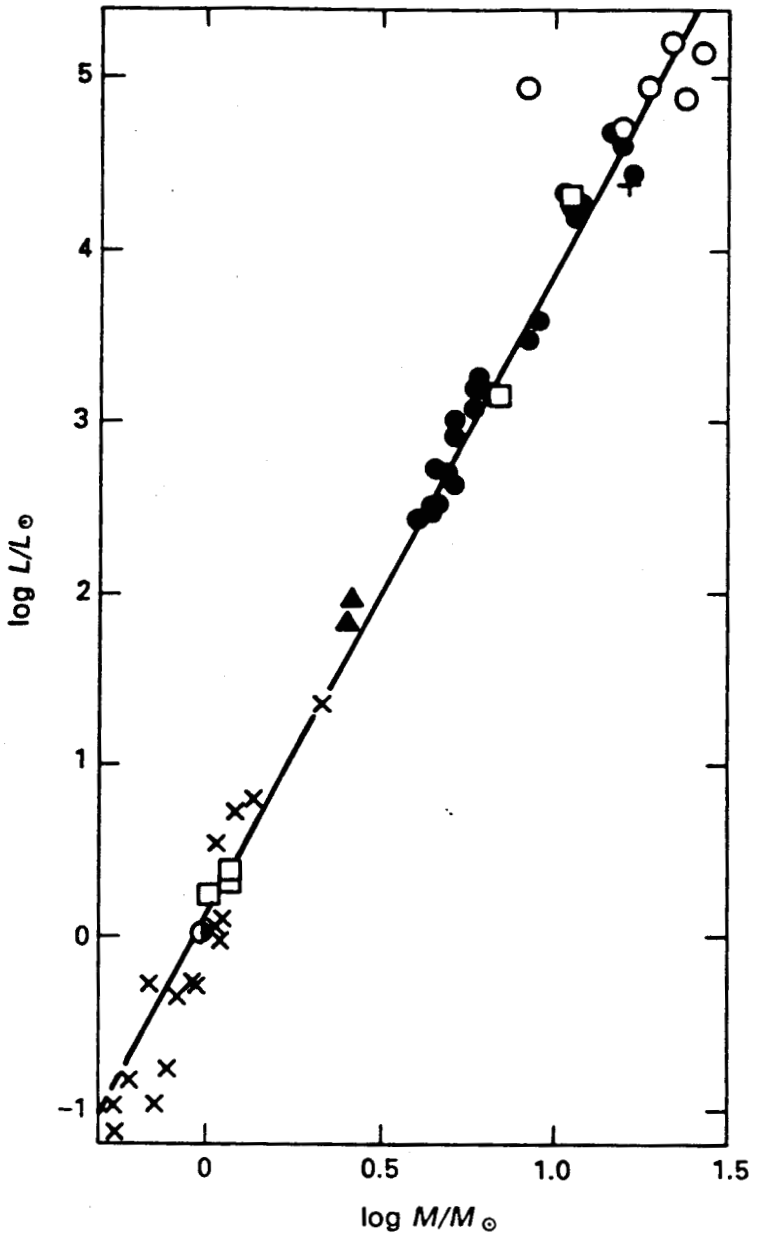

Fig. 1.13. The relation between stellar luminosities and stellar masses for binaries with well determined masses. The different symbols refer to different kinds of binaries. From Popper (1980).

Fig. 2

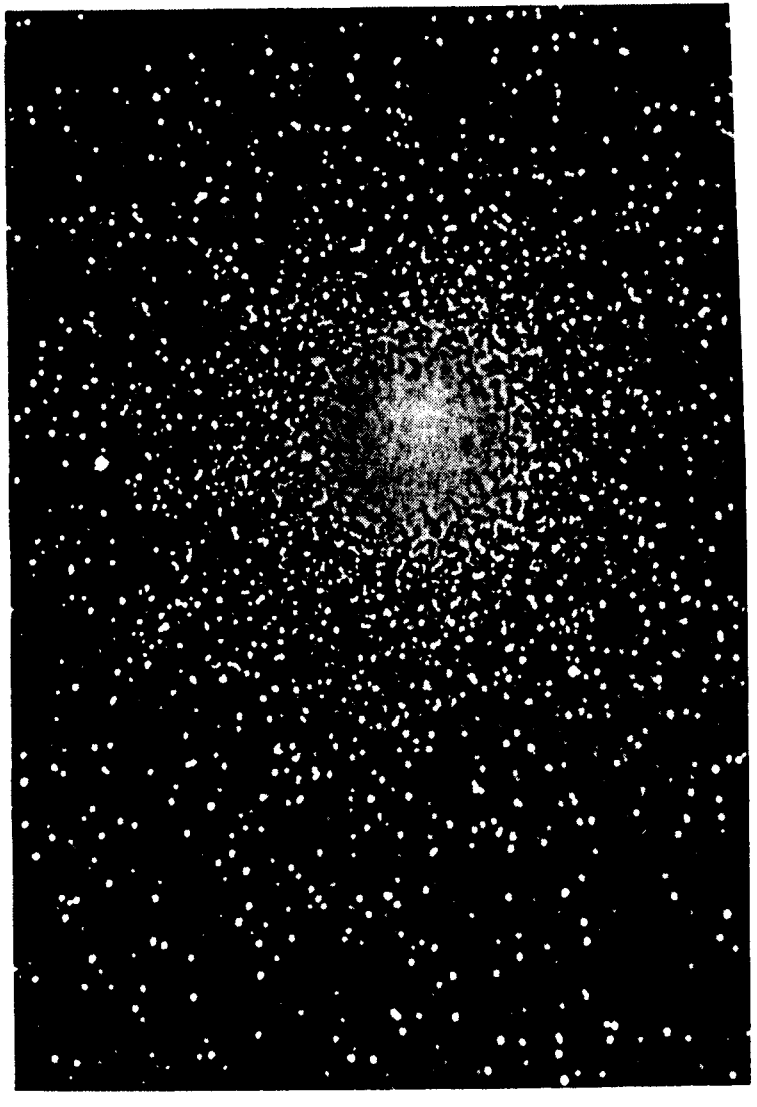

A photograph of the globular cluster 47 Tucanae. From Burnham (1978c).

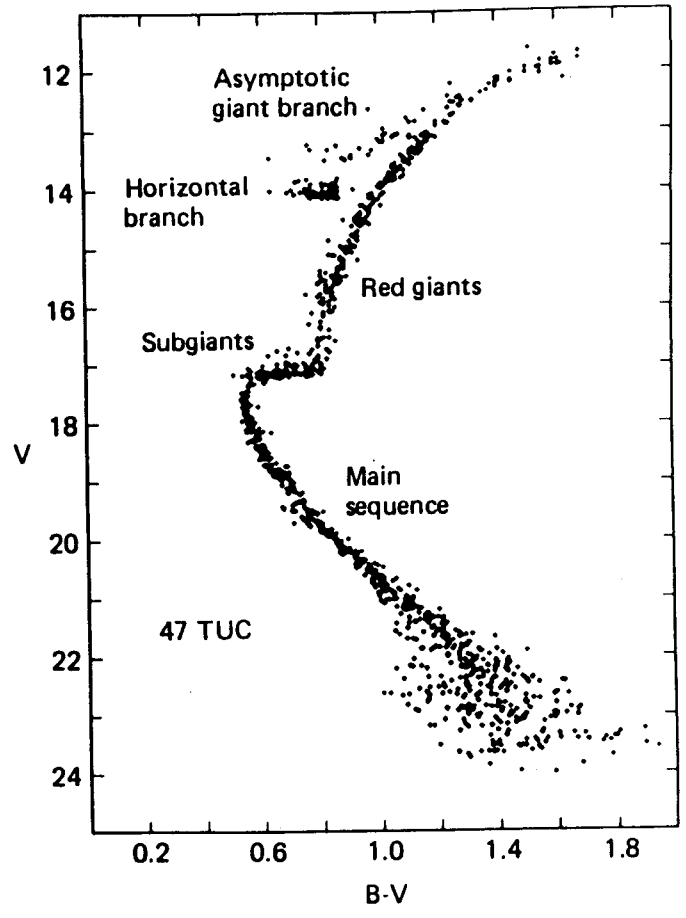

Fig. 1.7. The color apparent magnitude diagram for 47 Tucanae. The new measurements go down to stars as faint as 23rd magnitude, though for the faint stars the scatter becomes large. The main sequence and the giant and subgiant branches are surprisingly sharp, showing that there are very few or no binaries in this globular cluster. The red stub of the horizontal branch is seen at $V \sim 14$ and $B - V \sim 0.8$. The asymptotic giant branch (see Chapter 14) is seen above the horizontal branch. From Hesser *et al.* (1987).

Fig. 3

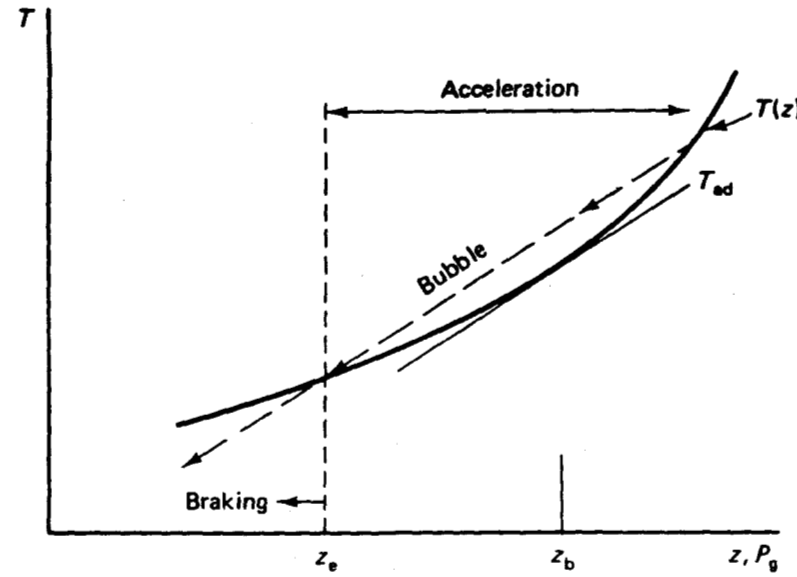

Fig. 6.6. Shows schematically the temperature stratification $T(z)$ of the stellar atmosphere at the surface of the convection zone (thick solid line) and the adiabatic temperature stratification (thin solid line). The upper boundary of the convection zone occurs at the depth z_b where $dT/dz = (dT/dz)_{ad}$. A rising bubble may follow the path indicated by the dashed line. At the upper boundary of the convection zone at z_b the bubble still has $\Delta T > 0$ and is still being accelerated up to the depth z_e, for which $\Delta T = 0$. Due to its inertia it still continues to move upwards but obtains now $\Delta T < 0$ and is braked. It finally comes to rest at a point $z_0 < z_e$, i.e. much higher than the upper boundary of the convection zone. Energy exchange reduces the overshoot distance.

Fig 13

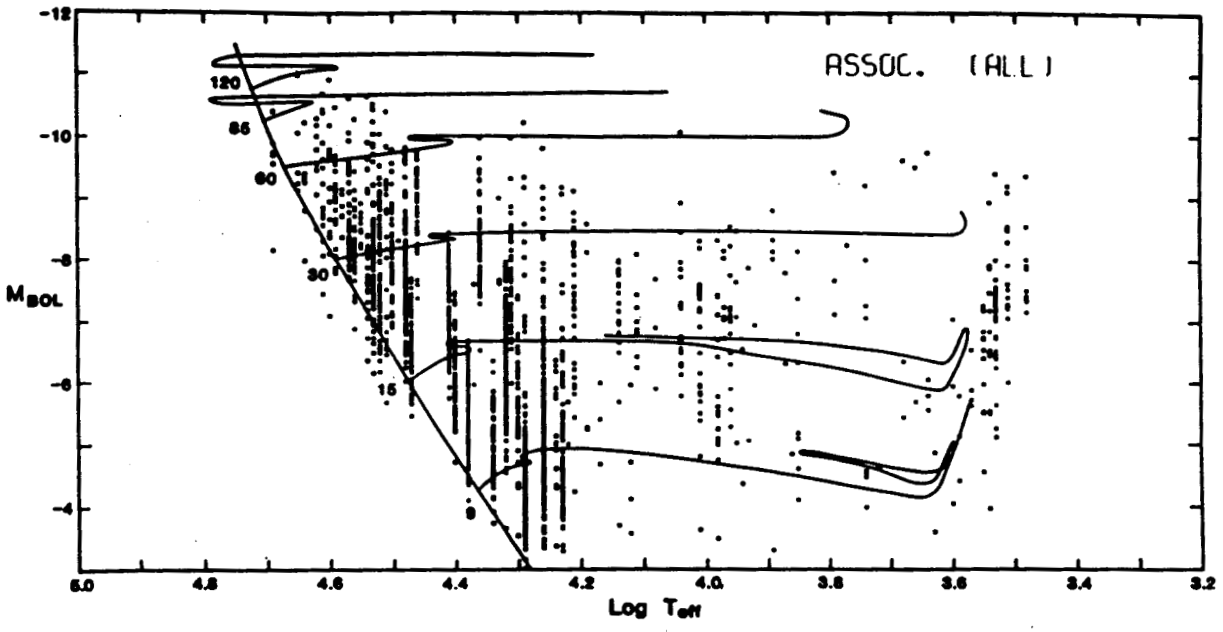

Figure 1 - The HR diagram, M_{Bol} vs. log T_{eff}, for O-type stars, supergiants, and less luminous early-type stars in 91 stellar associations and clusters in the solar region of our Galaxy.

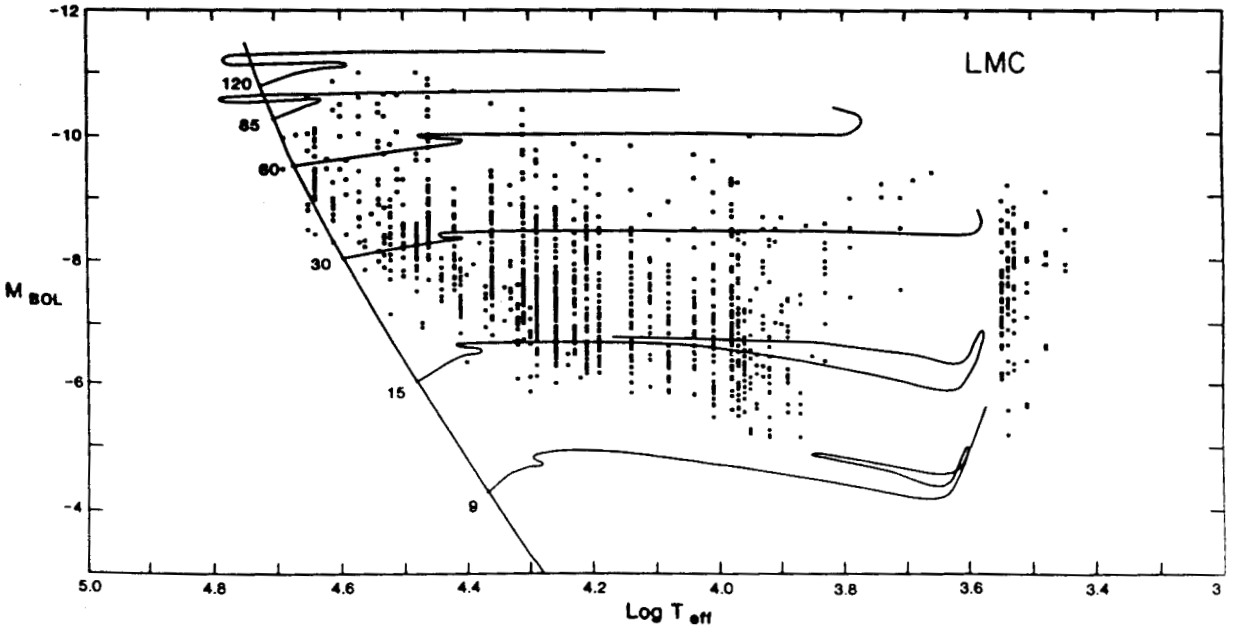

Figure 2 - The M_{Bol} vs. log T_{eff} diagram for confirmed and suspected luminous stars in the Large Magellanic Cloud.

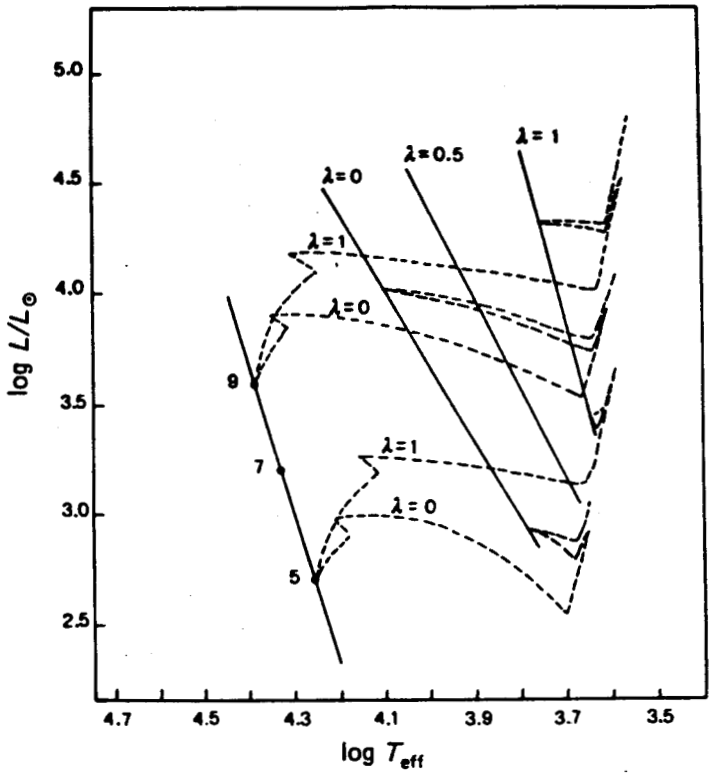

Fig. 11

Fig. 15.3. Compares evolutionary tracks of stars with $M = 5\ M_\odot$ and $M = 9\ M_\odot$ for the same chemical composition but with different degrees of mixing during the main sequence phase. With more mixing ($\lambda = 1$ means overshoot by 1 pressure scale height) in the core of main sequence stars, the luminosity of the giant phase is increased as compared to no overshoot mixing ($\lambda = 0$). The luminosity for the blue loop is further increased. The solid lines on the right connect the tips of the blue loops for the different mixing parameters λ. The solid line on the left shows the main sequence. From Bertelli, Bressan and Chiosi (1984).

BÖHM-VITENSE ET AL.

Ap J Vo

FIG. 7.—Luminosities at the tips of the blue loops shown as a function of stellar masses. The different curves are for different evolutionary tracks assuming different amounts of convective overshoot mixing. The Becker (1981) models assume no overshoot. The models of Maeder & Meynet (1988) assume convective overshoot mixing by 0.25 pressure scale height, and those by Bertelli et al. (1986), who calculate the convective overshoot mixing for $\lambda = l/H = 1$, l = mixing length and H = pressure scale height. Also shown are the positions of V636 Sco and the other Cepheids with blue main-sequence companions, for which the dynamical masses have been determined by means of *HST* observations of their companions (*filled circles*), for S Mus (by Böhm-Vitense et al. 1997a), for V350 Sgr (by Evans et al. 1997), for U Aql (by Evans et al. 1997b), for Y Car (by Böhm-Vitense et al. 1997b). The filled square gives the position of the new beat mass for Y Car. The position of SU Cyg, in a triple system, studied by Evans & Bolton (1990), is shown by the open circle. The vertical arrows indicate the change in luminosity if the Cepheid distances are increased by 10%, as suggested by Feast & Catchpole (1997).

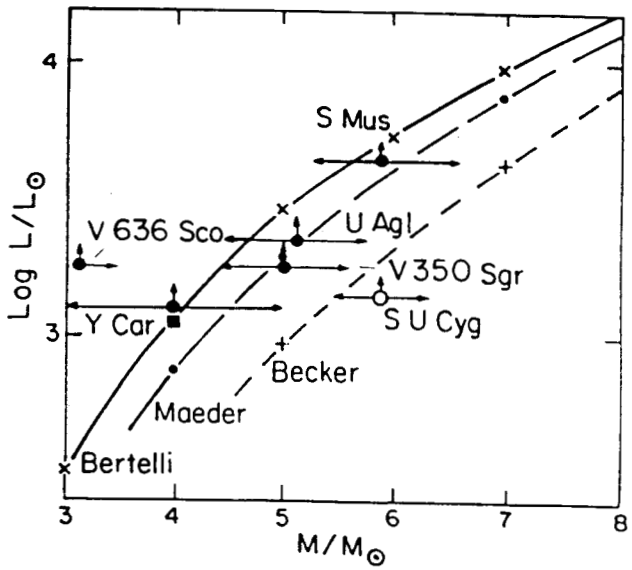

Fig 12

E.B.-V.

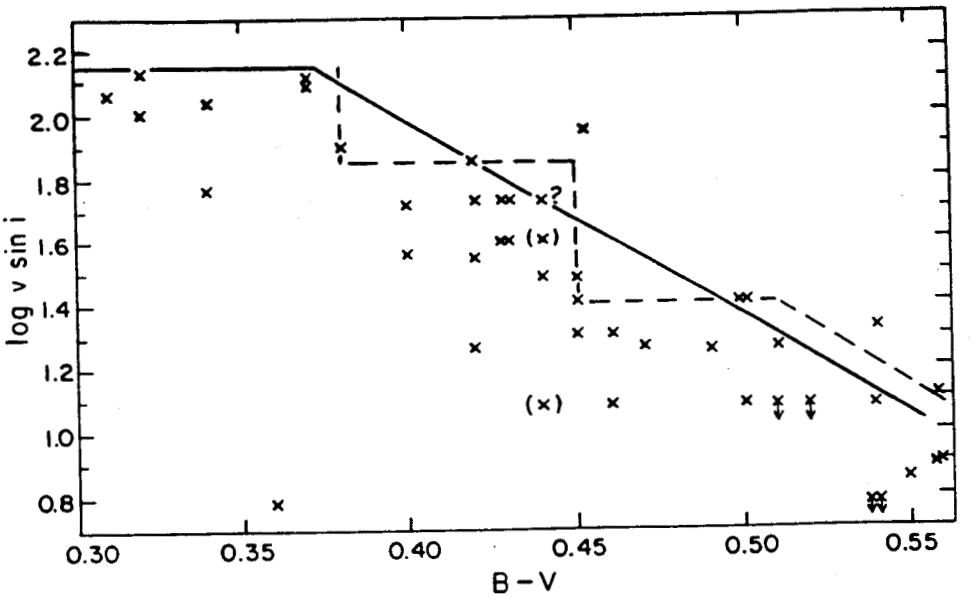

Fig 2

Gray, D.
+ Nagar, P.
ApJ 298, 756
1985

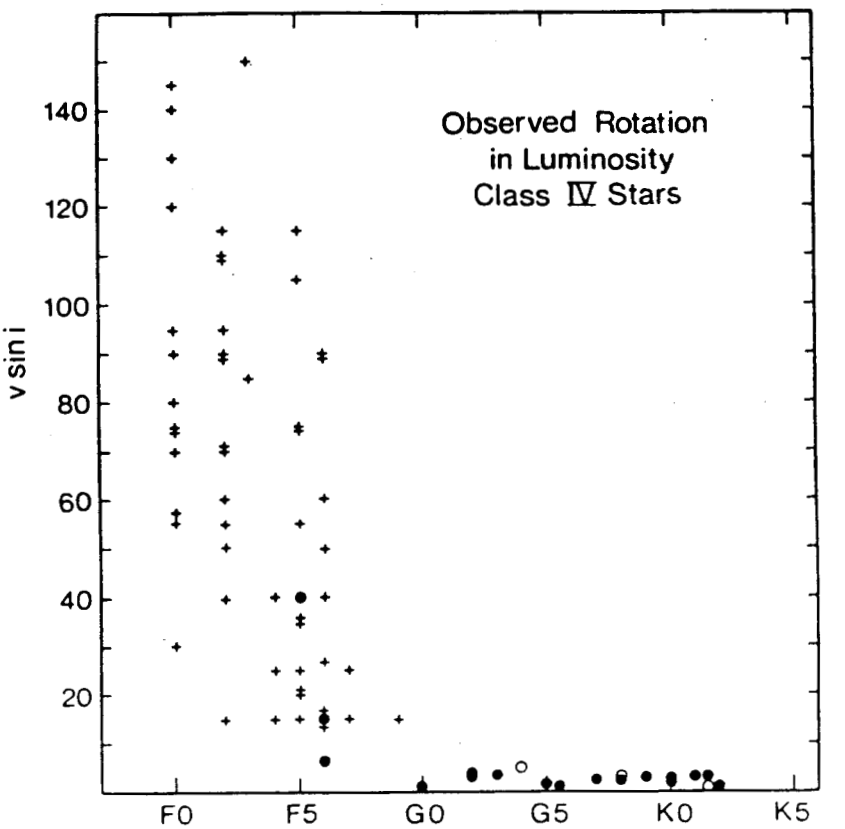

Gray Fig. 2

Fig

A + A
297, L25
E. B.-V.

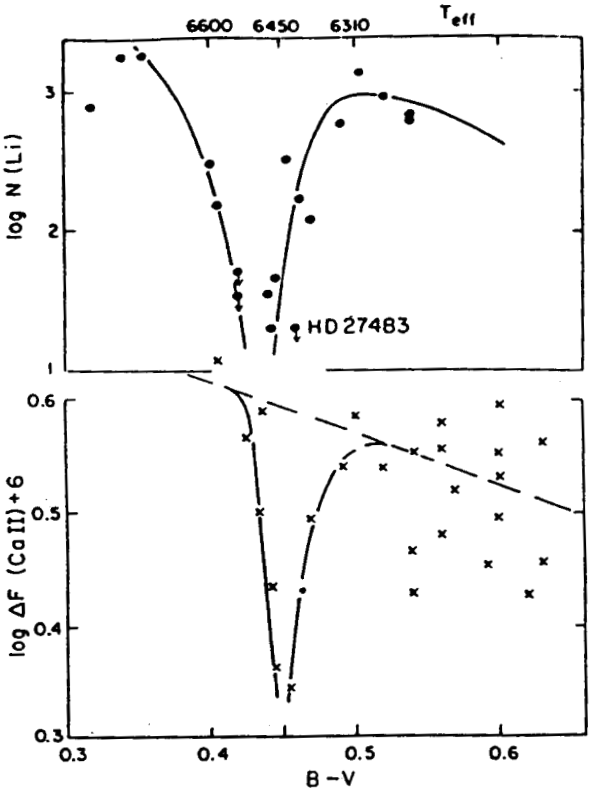

Fig 15

Figure 2. The dip in the CaII surface emission line fluxes at B-V=0.45 is compared with the dip in the Li surface abundances for the Hyades main sequence stars. The average Δ F(B-V) relation is shown by the dashed line. (The T_{eff} scale according to Bohm-Vitense 1981, is given at the top.) The branch of the Δ F dip with decreasing ΔF for increasing B-V is shifted to larger B-V values than for the Li dip, shifting the center of the Δ F dip by Δ B-V=0.01 as compared to the Li dip, corresponding to a shift in temperature of ≤90 K. HD27483 is a triple system with a hot WD. The dot indicates the Wilson measurement for the one star whose B-V falls within the range of the dip.

E. B.-V.
unpublished

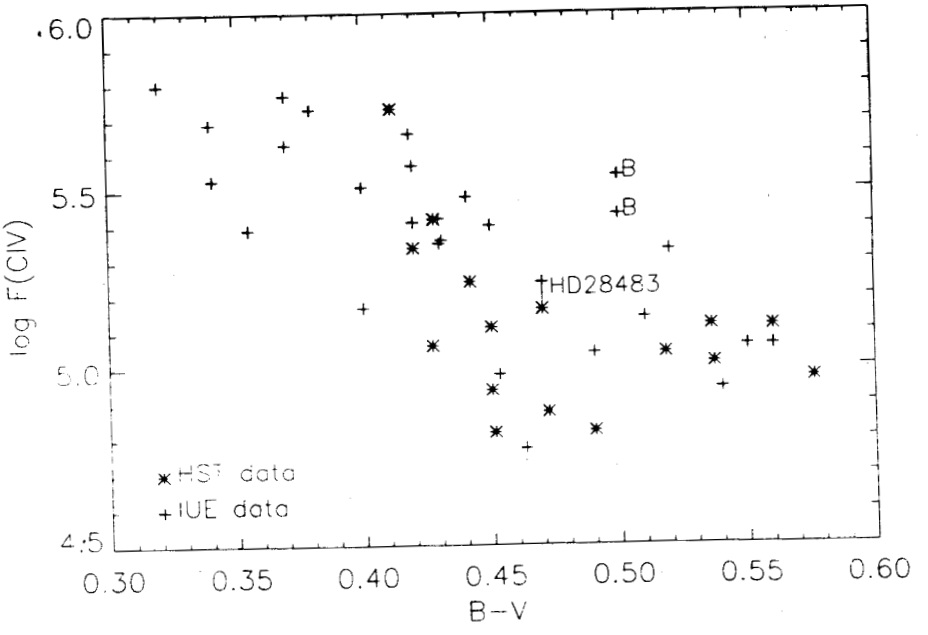

Fig. 21.1. Circulation in a rotating star.

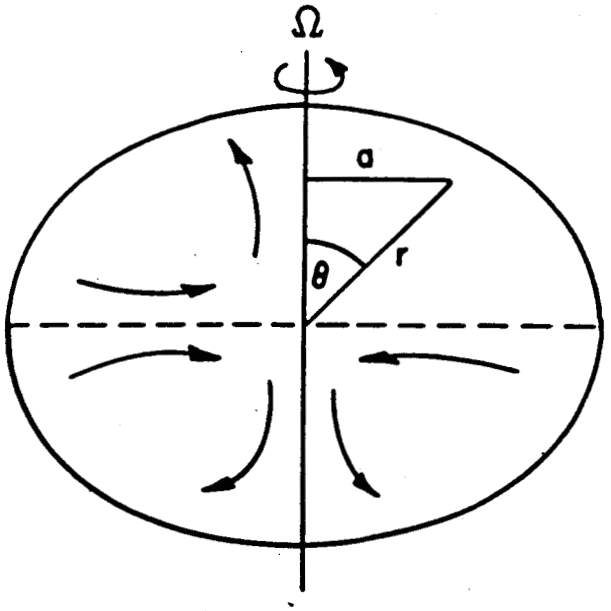

Fig 14

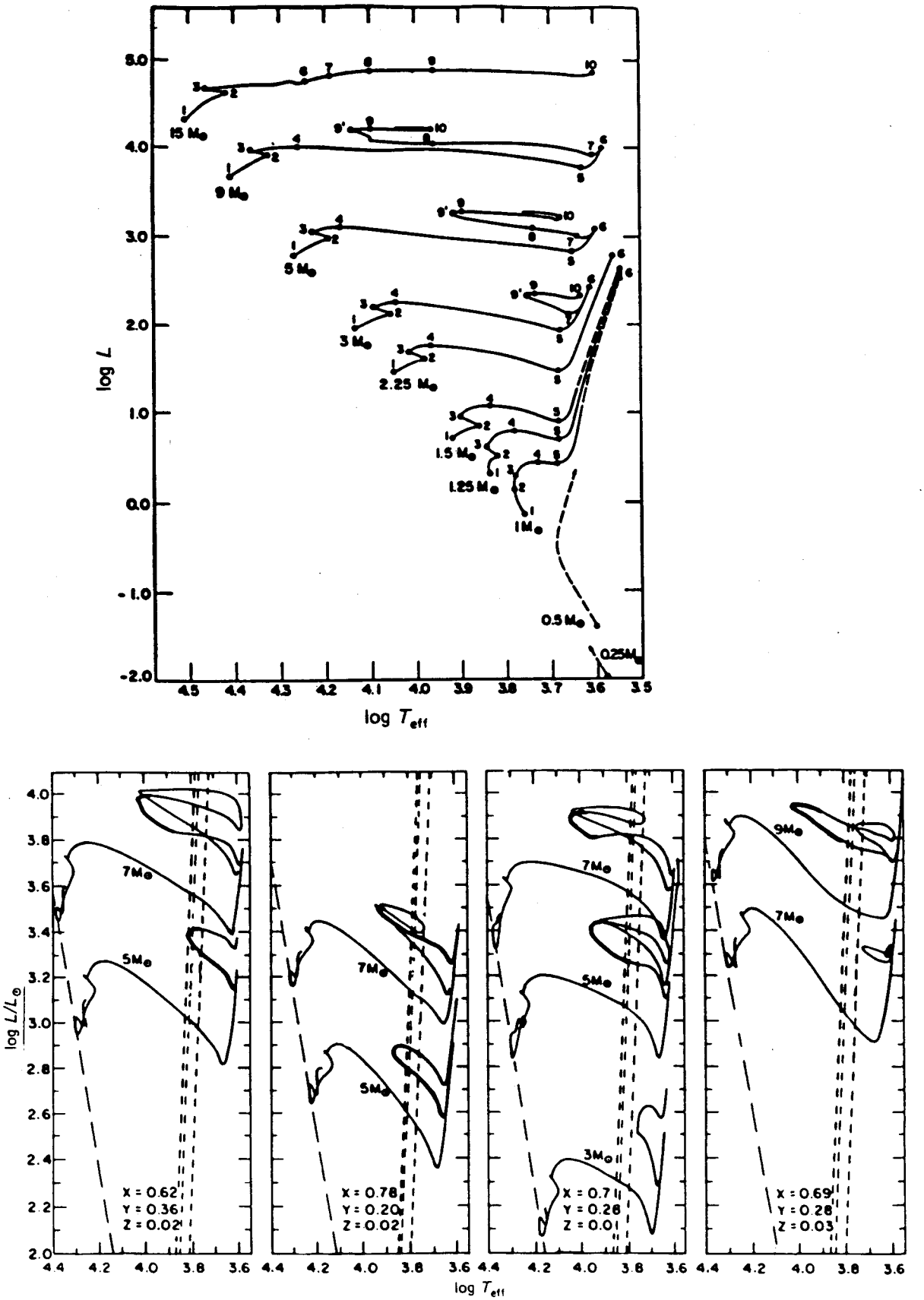

Fig. 15.2. During advanced stages of evolution, massive stars with $M > 3\ M_{\odot}$ make several blue loop excursions when new nuclear reactions become possible in their cores. The luminosities and the extent of the blue loops depend on the chemical composition, as may be seen from comparing the different panels. The abundances used are given in the panels. An increased helium abundance increases the luminosities. An increased abundance of heavy element decreases the luminosities and shortens the loops. The nearly vertical dashed lines show the Cepheid instability strip (see Chapter 17). Adapted from Becker, Iben and Tuggle (1977).

Hydrogen Burning Cont.

CNO cycle, $\sim 10^7$ K

$C^{12} + H^1$	$\rightarrow$	$N^{13} + \gamma$	10^6 years
N^{13}	$\rightarrow$	$C^{13} + e^+ + \nu$	14 min
$C^{13} + H^1$	$\rightarrow$	$N^{14} + \gamma$	3×10^5 years
$N^{14} + H^1$	$\rightarrow$	$O^{15} + \gamma$	3×10^8 years
O^{15}	$\rightarrow$	$N^{15} + e^+ + \nu$	82 sec
$N^{15} + H^1$	$\rightarrow$	$C^{12} + He^4$	10^4 years

or

$$N^{15} + H^1 \rightarrow O^{16} + \gamma$$

$$O^{16} + H^1 \rightarrow F^{17} + \gamma$$

$$F^{17} \rightarrow O^{17} + e^+ + \nu$$

$$O^{17} + H^1 \rightarrow N^{14} + He^4$$

triple α process = helium burning

$$He^4 + He^4 \leftrightarrow Be^8$$

$$Be^8 + He^4 \rightarrow C^{12} + 2\gamma + 7.6 \text{ MeV} \quad T \sim 10^8 \text{ K}$$

but $He^4 + He^4 \leftrightarrow Be^8 - 95$ keV

Li problem

$$Li^6 + H^1 \rightarrow He^4 + He^3 \quad \text{at } T \sim 2 \times 10^6 \text{ K}$$

$$Li^7 + H^1 \rightarrow 2He^4 \quad \text{at } T \sim 2.4 \times 10^6 \text{ K, i.e., deeper layer}$$

Table 9.1 *Masses and radii for some visual binaries according to D. Popper (1980)*

Star	S_p	$M/M_\odot$	$R/R_\odot$	π''
α CMaA	A1 V	2.20	1.68	0.377
α CMi	F5IV-V	1.77	2.06	0.287
ξ Her A	G0IV	1.25	2.24	0.104
ξ Her B	K0V	0.70	0.79	0.104
α Cen	G2V	1.14	1.27	0.743
γ Vir	F0V	1.08	1.35	0.094
η Cas A	G0V	0.91	0.98	0.172
η Cas B	M0V	0.56	0.59	0.172
ξ Boo	G8V	0.90	0.77	0.148

Fig 5a

Convective Instability

Schwarzschild criterion:

$$\nabla_{\rm ad} = \left(\frac{d\ln T}{d\ln P}\right)_{\rm ad} < \left(\frac{d\ln T}{d\ln P}\right)_{\rm rad} = \nabla_{\rm rad} \tag{7}$$

If

$$E = E_{\rm kin} = \frac{3}{2}kT, \qquad C_v = \frac{3}{2}R_g, \qquad C_p = \frac{5}{2}R_g, \qquad \text{and} \qquad \gamma = \frac{5}{3} \tag{8}$$

$$\nabla_{\rm ad} = \frac{\gamma - 1}{\gamma} = 0.40 \tag{9}$$

For radiative equilibrium

$$\frac{dT}{dr} = -\frac{\pi F_{\rm rad}}{\sigma}\frac{3}{16}\frac{\kappa_{\rm cm}}{T^3} \qquad\qquad \frac{d\ln P}{dr} = -\frac{1}{H_{\rm p}} \tag{10}$$

$$\nabla_r = \frac{d\ln T}{d\ln P} = \pi F \cdot \frac{3}{16} \cdot \frac{\kappa_{cm}}{\sigma T^4} \cdot H_p = \frac{3}{16}\left(\frac{T_{\rm eff}}{T}\right)^4 \cdot \frac{\kappa_g P}{g} \tag{11}$$

Reasons for Convective Instability

1) Small $\nabla_{\rm ad}$ in H and He ionization regions

2) Large $\nabla_{\rm rad}$ for large F in interiors of massive stars

3) Large increase in κ when H starts to liberate electrons to make H^-, and also $\kappa(H)$ increases

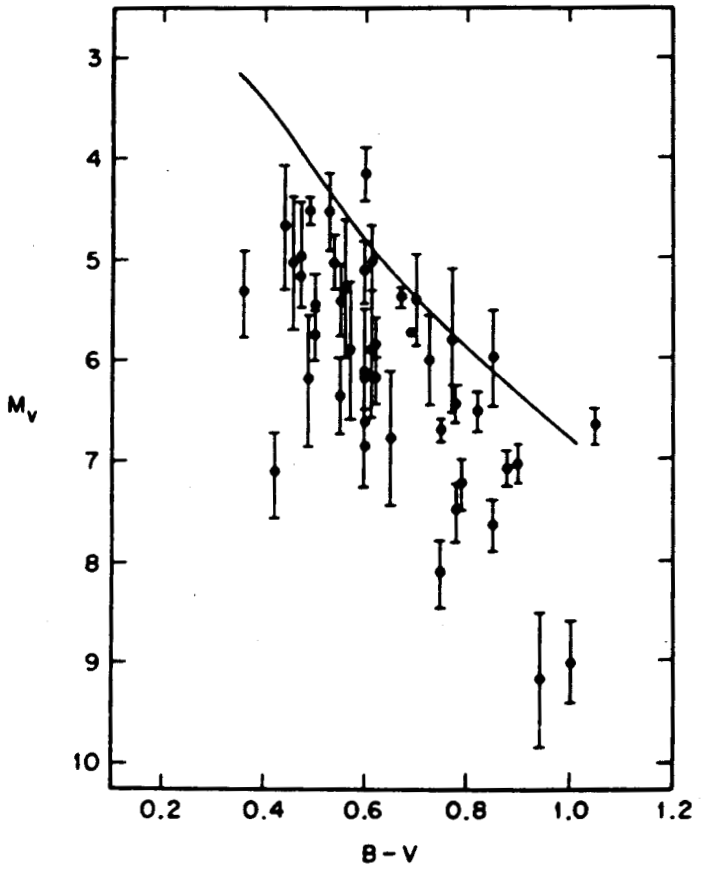

Fig. 10.9. The color magnitude diagram for the nearest population II stars, for which trigonometric parallaxes can be measured. The vertical lines indicate error bars. The solid line shows the main sequence for stars with solar element abundances. When compared at the same B − V the main sequence for very metal-poor stars appears to be about two magnitudes below the solar abundance main sequence. When compared at equal T_{eff} the difference is smaller, because for a given T_{eff} the B − V decreases for metal-deficient stars. From Sandage (1986).

Radiative Energy Transport

$$F_r = \frac{16}{3}\frac{\sigma}{\pi}T^3 \cdot \frac{1}{\kappa_{cm}} \cdot \frac{dT}{dr}$$

$$\left(F_r = \frac{4}{3}\frac{dB}{d\tau}\right) \qquad \text{with} \quad d\tau = \kappa_{\mathrm{cm}} dr$$

If only radiative energy transport

$$L \propto 4\pi R^2 \cdot \pi F_{rad} \propto -\frac{T^3}{\kappa_g \rho} \cdot \frac{dT}{dr} R^2$$

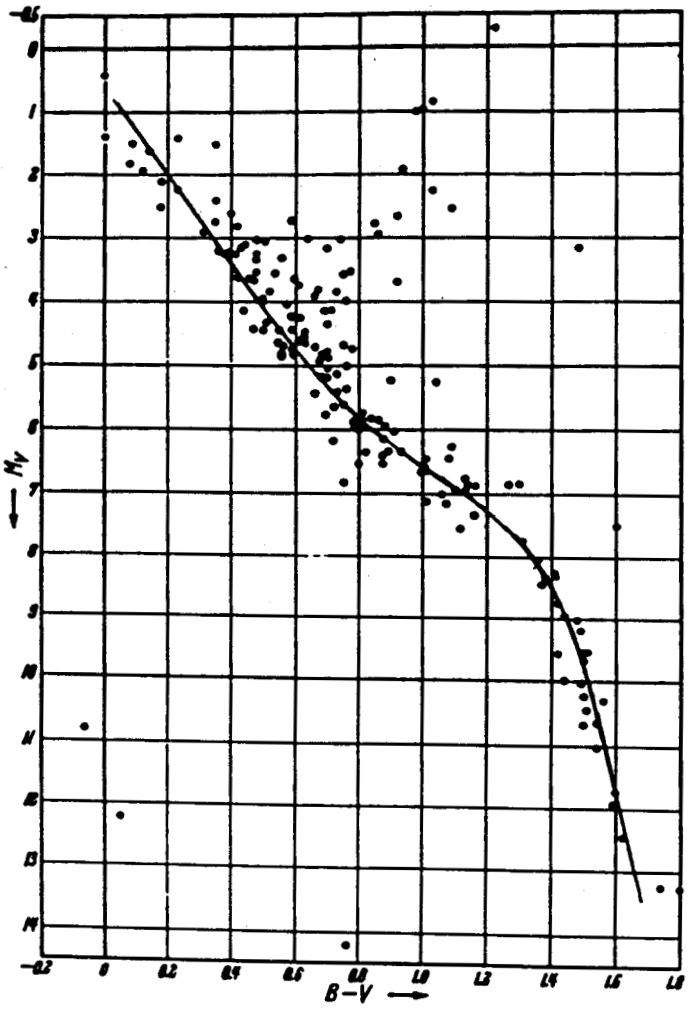

Fig. 1. The color magnitude diagram for nearby stars is shown according t Johnson and Morgan (1953). For better comparison with the following color magnitude diagrams we have added an eye-fitted average curve for the main sequence stars.

Fig 1

Energy Gain

Hydrogen burning

$$m(H^1) = 1.007852 \qquad 4 \cdot m(H^1) = 4.031408$$

$$m(He^4) = \qquad \underline{4.002603}$$

$$\Delta m = \qquad 0.028805$$

$$\frac{\Delta m}{m} = \qquad 7 \times 10^{-3}$$

Helium burning

$$3 \cdot m(He^4) = 3 \cdot 4.002603 = 12.007809$$

$$m(C^{12}) = \qquad \underline{12.000000} \qquad \text{per definition}$$

$$\Delta m = \qquad 0.007809$$

$$\frac{\Delta m}{m} = \qquad 6.575 \times 10^{-4} \qquad 10\% \text{ of gain}$$

for H burning

(18)

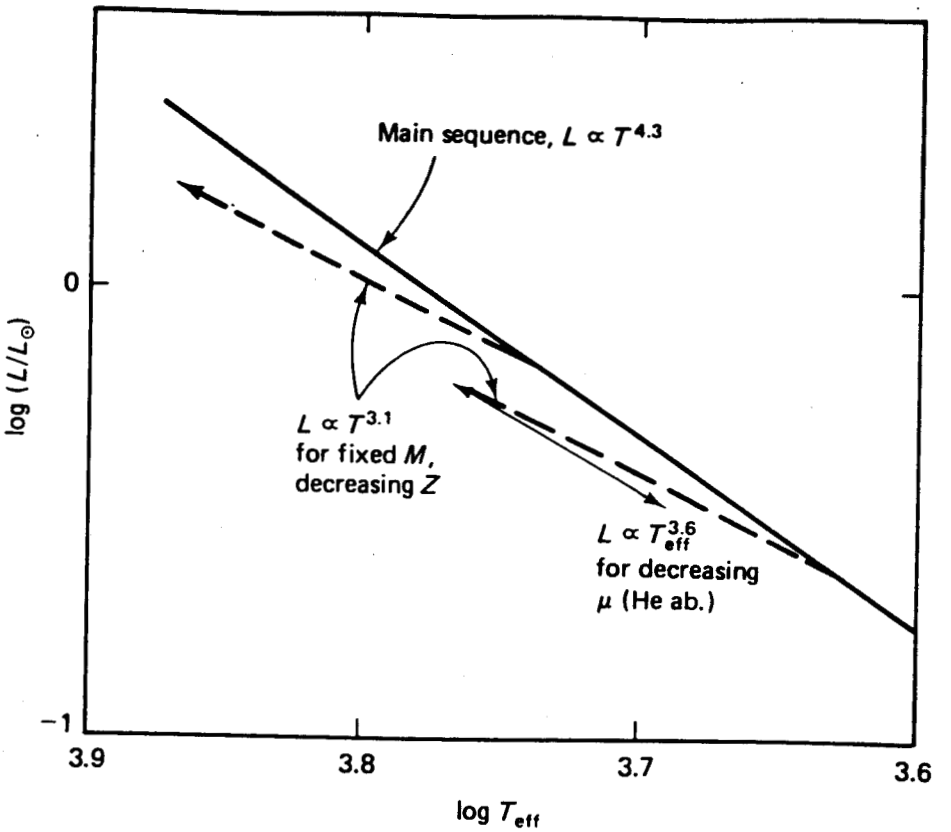

E. B. -V

Fig 6

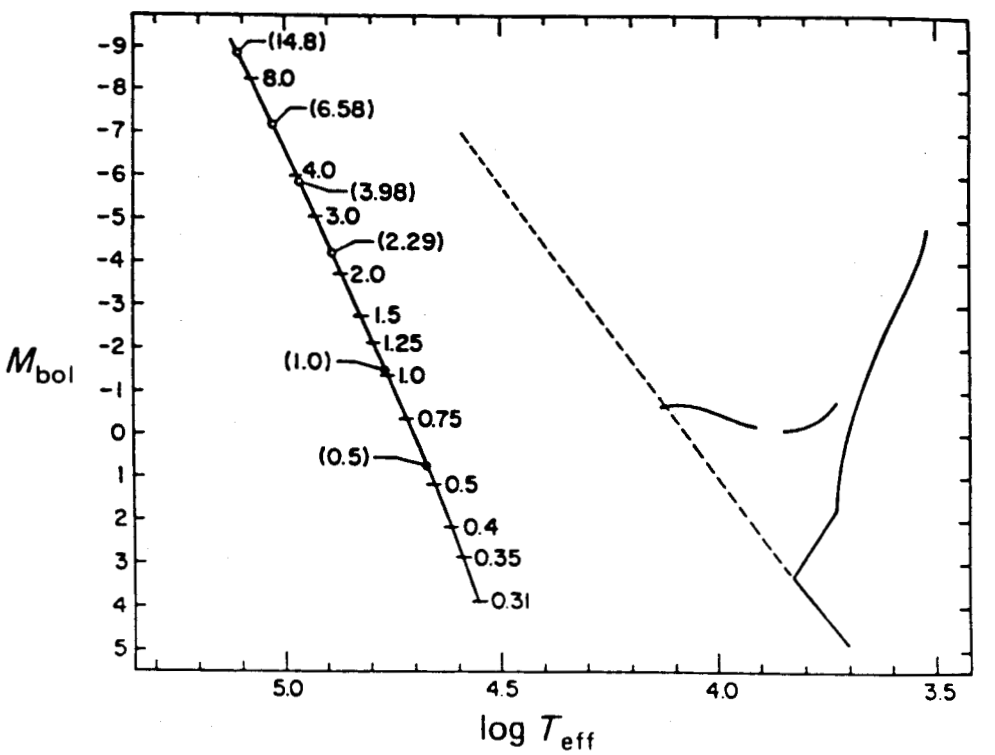

Fig. 10.7. In the M_{bol}, T_{eff} diagram the main sequence for hydrogen stars (das is compared with the main sequence for helium stars as calculated by Cox and The stellar masses in units of solar masses are given at the appropriate points. circles are from less accurate calculations.) Also shown in the lower right is a cluster diagram for comparison. From Cox and Salpeter (1964).

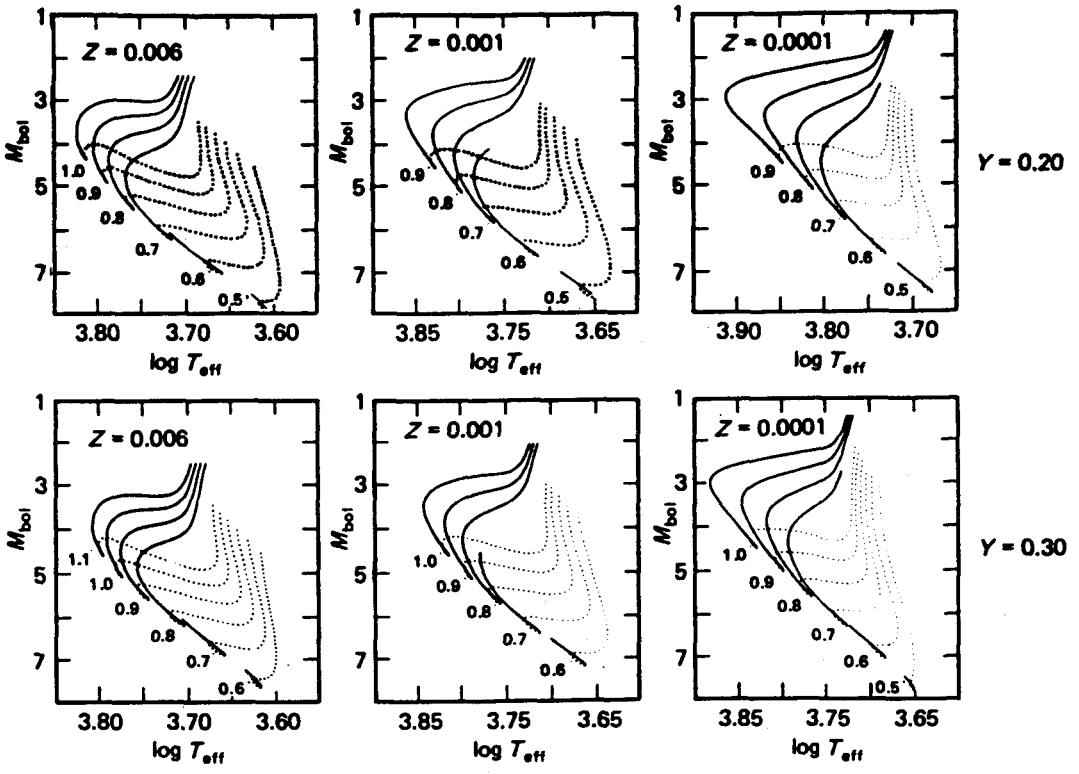

Fig. 10.10. In the M_{bol}, log T_{eff} diagram main sequences for different metal abundances Z and helium abundances are shown. A helium abundance $Y = 0.30$ was assumed for the lower panel and $Y = 0.20$ for the upper panel. Stellar masses (in units of the solar mass) are given at the point of arrival on the main sequence. These points outline the so-called zero age main sequence (ZAMS). The shift of stellar positions for a given mass to higher T_{eff} and L for increasing Y and decreasing Z is obvious. Note the change in the T_{eff} scale for the different panels. The dotted lines outline the evolution during the contraction phases (see also chapter 11). From VandenBerg and Bell (1985).

Fig

Consequences of Hydrostatic Equilibrium

Rough estimates

$$\frac{dP}{dr} = -\rho \cdot \frac{GM_r}{r^2} \qquad \Longrightarrow \qquad \frac{P}{R} \propto \frac{M}{R^3} \cdot \frac{M}{R^2} \propto \frac{M^2}{R^5}$$

$$\mathbf{P} \propto \frac{\mathbf{M^2}}{\mathbf{R^4}}$$

$$T \propto \frac{P}{\rho} \propto \frac{M^2}{R^4}\frac{R^3}{M} = \frac{\mathbf{M}}{\mathbf{R}} \propto \mathbf{T}$$

$$\underline{L} \propto \frac{T^4}{\kappa} \cdot \frac{R^3}{M} \cdot R^2 \propto \frac{M^4}{R^5} \cdot \frac{R^5}{M} \propto \underline{M^3} \qquad \text{if} \quad \kappa_g = \text{const.}$$

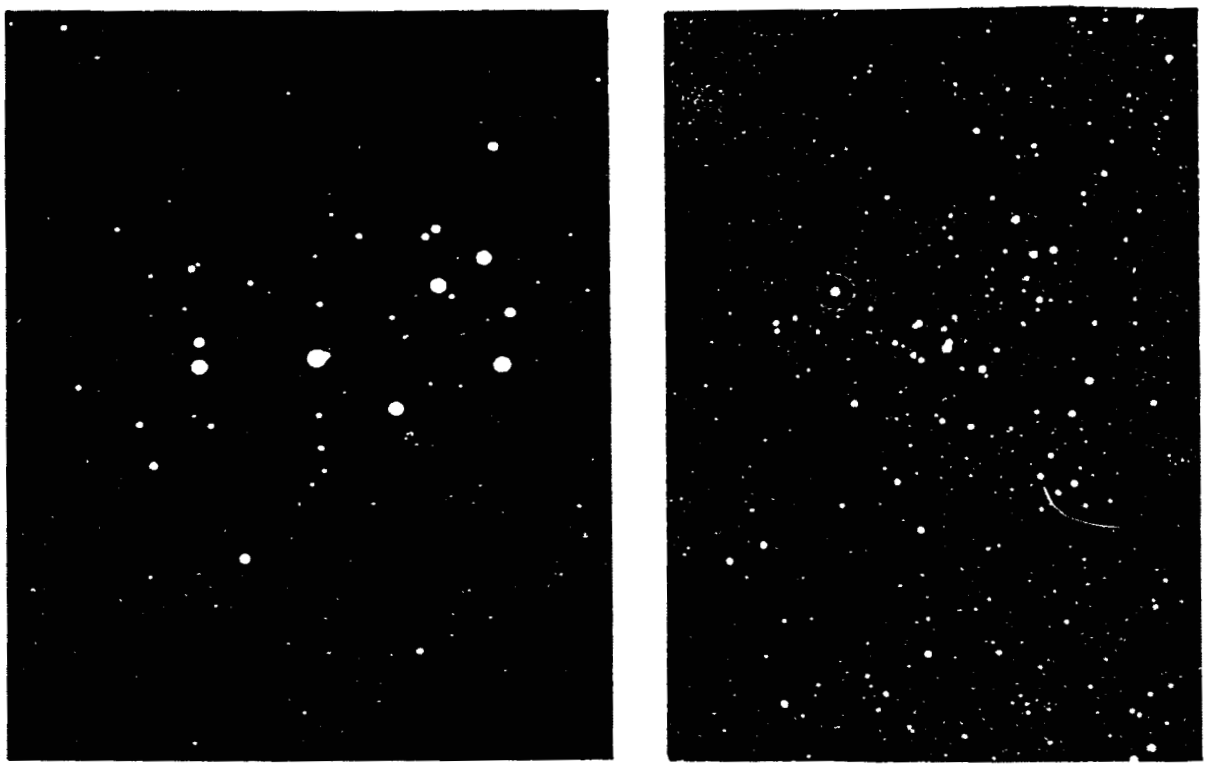

(a) (b)

Fig. 5.2. Photographs of the well-known star clusters, the Pleiades (*a*), and the Hyades (*b*), in the constellation of Taurus. (From Burnham 1978.)

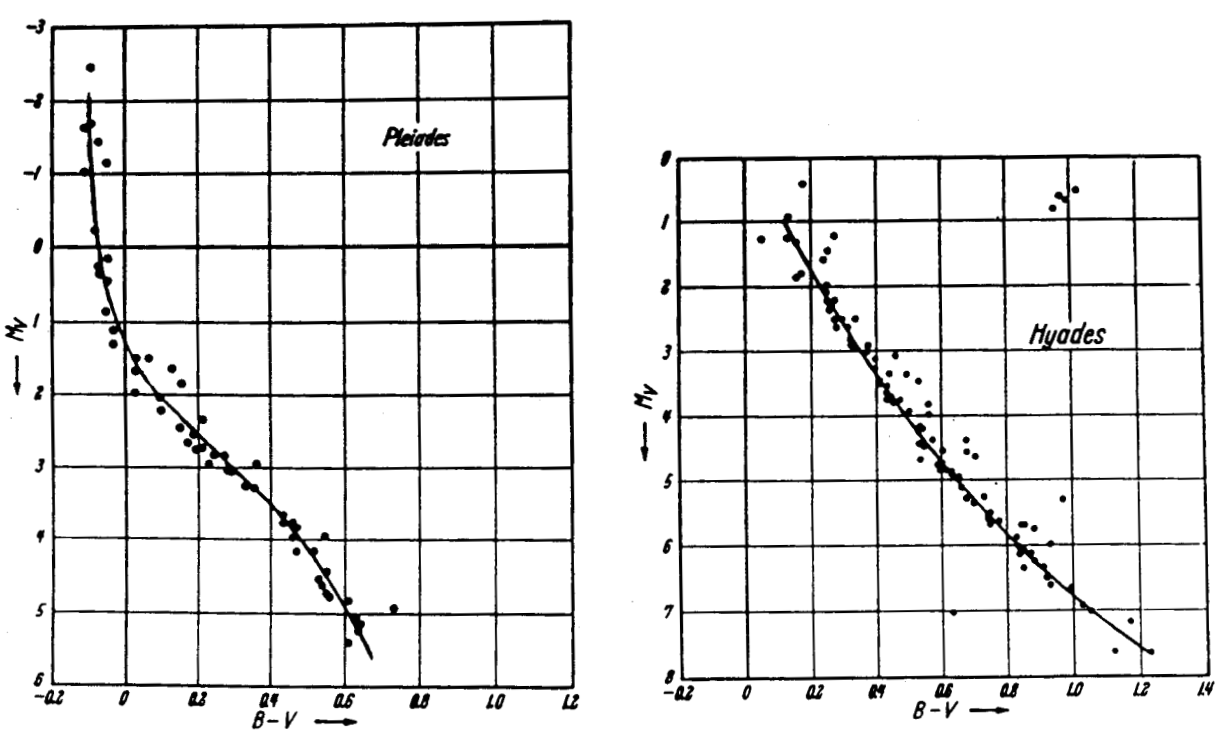

(a) (b)

Fig. ~~5.3~~ 2. The color, absolute magnitude diagrams for the Pleiades (*a*) and Hyades (*b*) star clusters are shown according to Arp (1958). A distance modulus $m_V - M_V = 5.3$ was used for the Pleiades. For the Hyades individual distance moduli were used, averaging $m_V - M_V = 3.08$. Distance moduli larger by 0.2 magnitudes would be considered more appropriate now.

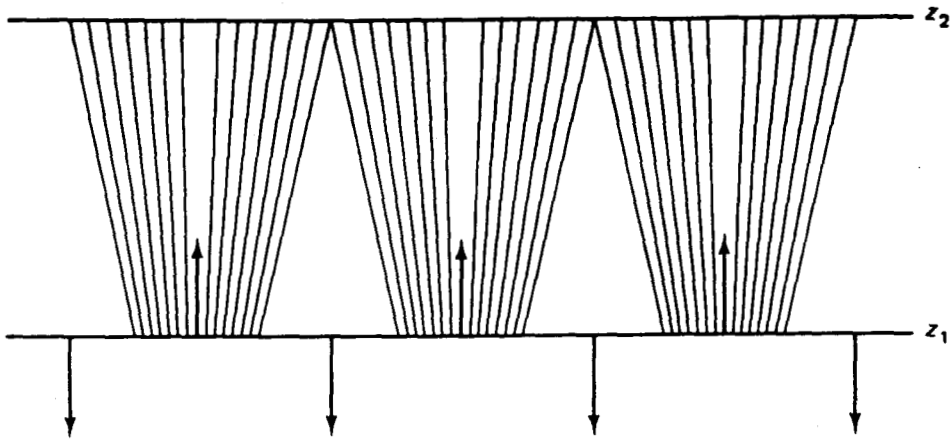

Fig. 6.4. In a layer at depth z_1 half the area is covered by rising bubbles and half by falling gas. The rising bubbles expand. They cover larger and larger areas. If in the layer at depth z_2 their cross-section has expanded by a factor of 2, no areas would be left for the falling gas. The volume of the rising gas expands by a factor of e over one scale height. The cross-section expands by a factor of 2 over a distance of about one density scale height. Most of the upwards traveling gas has to be diverted into the downward stream over this distance. The characteristic traveling distance l is therefore expected to be of the order of one scale height.

Fig 19

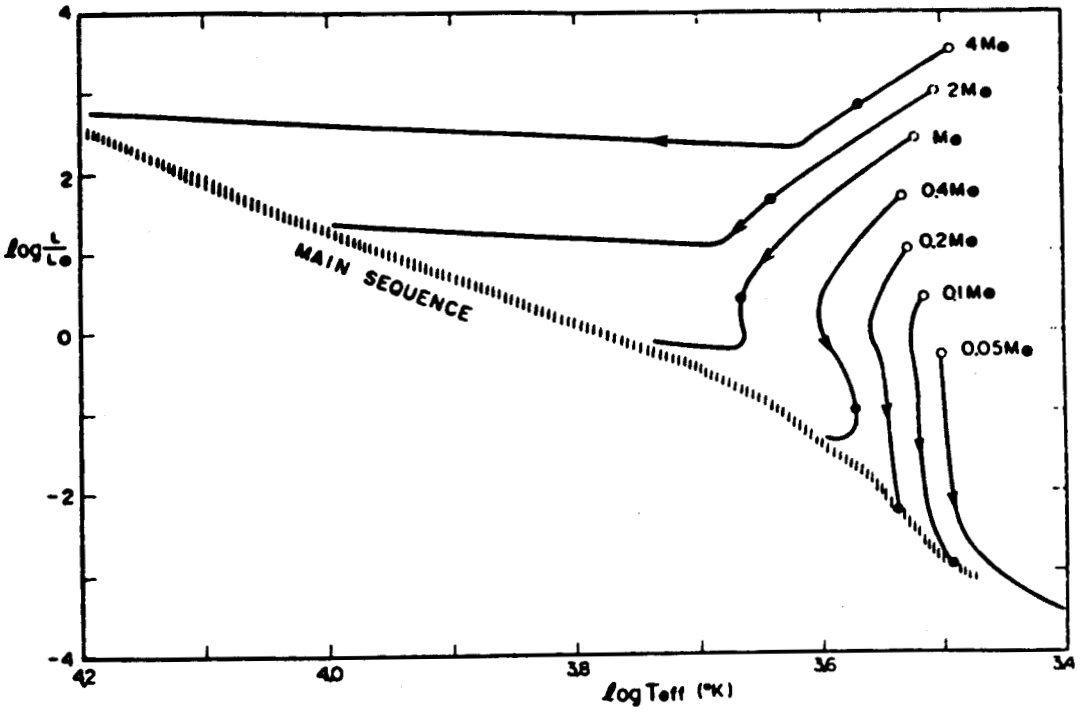

Fig. 20.8. In the log L, log T_{eff} diagram the contraction lines for different masses are shown, which first follow the Hayashi lines. The dots indicate the positions of homogeneous stars when they first arrive on the Hayashi line. From Hayashi (1966).

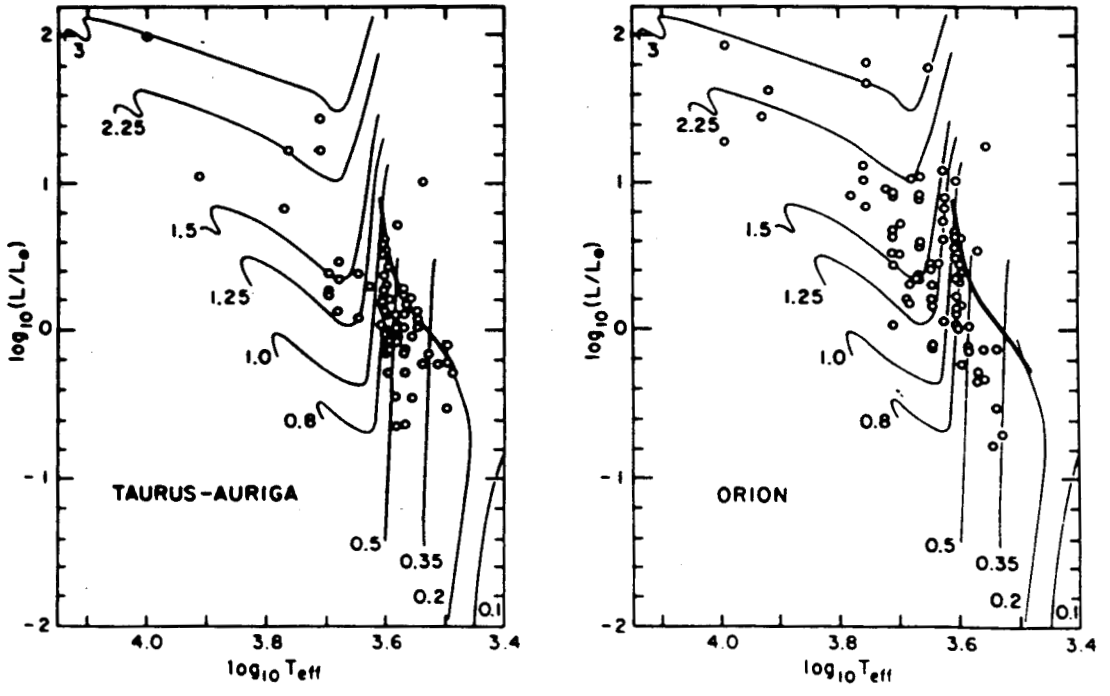

Fig. 20.9. The observed positions of young T Tauri stars in the Orion region and in the Taurus Auriga Association are shown in the L, T_{eff} diagram. Also shown are the Hayashi tracks for stars of different masses as given in the figure. A birth line for stars seems to be indicated. It is marked by a thick line. Hardly any stars are found on the cool side of this line. For a 1 $M_{\odot}$ star a birth luminosity of $\log L/L_{\odot} = 0.9 \pm 0.1$ seems to be indicated as compared to $\log L/L_{\odot} = 2.3$ estimated on Fig. 20.8. Of course, we do not know the masses of the observed T Tauri stars, which we would need to know for a quantitative comparison. The overall shape of the birth line resembles Hayashi's simple and rough estimate. From Stahler (1983).

Jean's Criterion

Equation of motion at the surface:

$$\frac{d^2r}{dt^2} = -\frac{GM}{R^2} - \frac{1}{\rho}\frac{dP}{dr} \qquad \text{with} \qquad P = \frac{\rho T}{\mu} R_g \tag{1}$$

$$\frac{d^2r}{dt^2} \leq 0 \qquad \Longrightarrow \qquad \mathrm{M} > \mathrm{M_{crit}} = \frac{1}{2}\frac{\mathrm{T}^{3/2}}{\rho^{1/2}}\left(\frac{\mathrm{R_g}}{\mu \mathrm{G}}\right)^{3/2} \tag{2}$$

For a given mass, $T \propto \rho^{1/3}$, for equilibrium.

For adiabatic contraction, $T \propto \rho^{\gamma-1}$.

Hydrostatic equilibrium:

$$\frac{\mathbf{dP}}{\mathbf{dr}} = -\rho \cdot \frac{\mathbf{GM_r}}{\mathbf{r^2}} \tag{3}$$

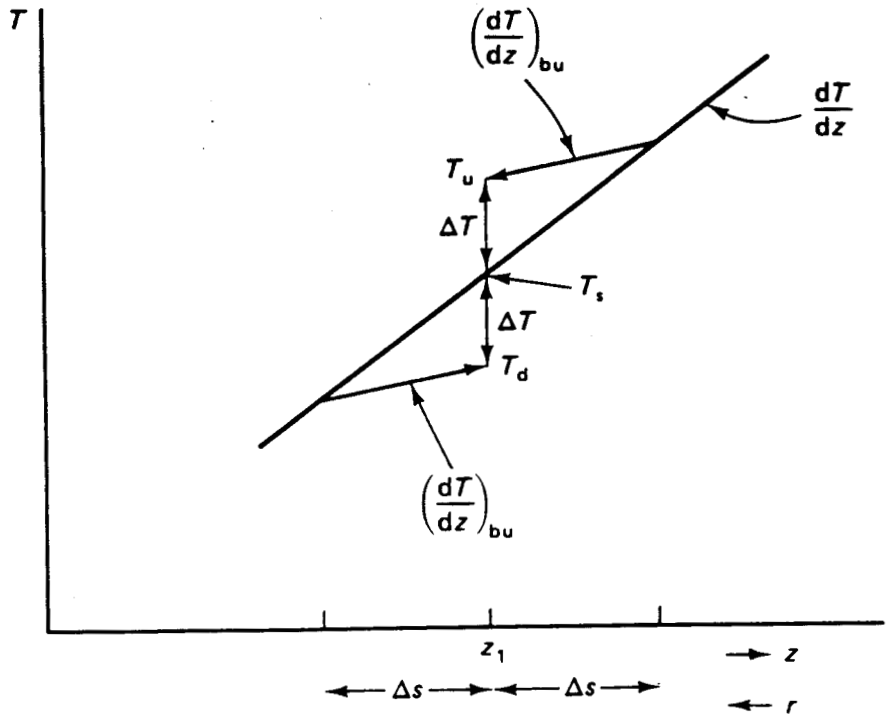

Fig. 6.2. In a given layer at depth z_1 we find gas traveling upwards as well as downwards with a temperature T_u or T_d respectively. T_s is the average temperature at depth z_1. For equal traveling distances Δz for the gas the difference $T_u - T_d = 2\Delta T$, with $\Delta T = T_u - T_s$ and also $\Delta T = T_s - T_d$. The subscript bu stands for gas bubble.

Fig. 3

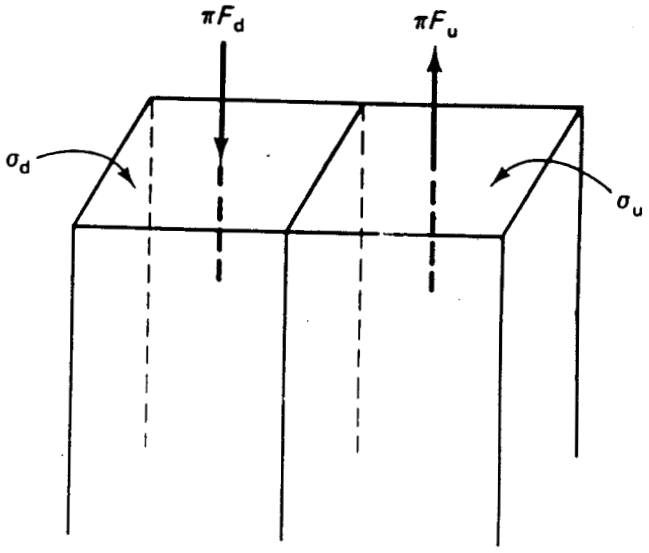

Fig. 6.1. Through a column with cross-section σ_u a stream of gas is flowing upwards, carrying an energy flux $\sigma_u \pi F_u$. Through another column with cross-section σ_d gas is flowing back down, carrying an energy flux $\sigma_d \pi F_d$.